

# ‘Discrete’ thinning dynamics in a continuum model of metallic nanowires

J. Bürki\*

*Department of Physics, University of Arizona, Tucson, AZ 85721*

(Dated: May 25, 2019)

Transmission electron microscopy experiments have recently observed gold metal nanocylinders to thin down in a discrete manner: A kink—a step of order one atomic layer—nucleates at one end and then moves along the wire, leaving a thinner cylinder behind it. In this paper, I show that a similar thinning process takes place within the nanoscale free-electron model, a structural and dynamical model of nanowires that treats the electron confinement effects exactly, while replacing the atomic structure by a continuum. Electron-shell effects, previously shown to be responsible for the very stability of wires with magic radii, favor the formation of kinks connecting magic cylinders. A rich kink dynamics, including interkink interactions, ensues, and is similar to that observed experimentally. Insights into the formation of kinks is gained through the study of the evolution of a locally perturbed non-magic cylinder, which is found to be a typical case of front propagation into an unstable state.

PACS numbers: temporary, 68.65.La, 66.30.Pa

The formation and thinning dynamics of metallic nanowires has been recently imaged, in real-time and with atomic resolution, using transmission electron microscopy (TEM).<sup>1,2,3,4,5</sup> Almost perfect Au<sup>1,2,5</sup> and Ag<sup>3,4</sup> cylindrical wires are found to form and be stable for seconds at room temperature. These cylinders usually do not break up at once, but are instead seen to thin down, one step at a time by an amount close to one atomic layer.<sup>5</sup> Real-time movies<sup>6</sup> of the thinning dynamics reveal that a kink structure nucleates at one end of the wire and subsequently moves along the cylinder. The kink formation and initial displacement are extremely rapid, of the order of the time resolution of the experiment, while subsequent motion is slower. In some cases, a kink appears to stop along the wire until it is joined by another step, at which point they move along together.

This dynamics involves hundreds, if not thousands, of atoms, and takes place over seconds. It is thus far beyond the reach of *ab initio*<sup>7</sup>, or classical molecular dynamics<sup>8</sup> simulations, which typically cover a few nanoseconds at most. Furthermore, due to the high number of surface atoms—with low coordination numbers—in such nanowires, surface effects are particularly important: Barring an additional stabilizing mechanism, they are expected to favor the development of a Rayleigh instability<sup>9</sup> that would break the wire up.<sup>10,11</sup> The stabilizing mechanism has been shown to come from electron-shell effects—similar to those well-known in cluster physics<sup>12</sup>—due to the quantum confinement of electrons in the cross-section of the wire. Any meaningful theoretical description of this problem thus requires a model that captures both surface and electron-shell effects. Furthermore, it needs to be simple enough to allow simulations of large systems over long timescales.

Both of these conditions are fulfilled by the nanoscale free-electron model (NFEM),<sup>10,13,14</sup> a continuum model where the atomic structure is replaced by a uniform, positively charged background, and the emphasis is put on the electronic structure. This model has successfully

explained the linear stability of cylindrical nanowires with radii in intervals of “magic” values as resulting from a competition between surface and electron-shell effects.<sup>11,15</sup>

The NFEM has been extended to include ionic dynamics through surface self-diffusion.<sup>14</sup> One of its important prediction is that a random wire naturally evolves into a universal equilibrium shape consisting of a perfect cylinder of a magic radius, connected to thicker leads.<sup>14,16</sup> A stochastic model of the dynamics of a nanowire under thermal fluctuations,<sup>17</sup> where cylinders are actually metastable states, has predicted long lifetimes compatible with experimental observations. The escape mechanism for long wires has been shown to consist of the nucleation of a kink at one end of the wire, which subsequently propagates and leaves a thinner or thicker cylinder.

Motivated by these results suggesting that a dynamics similar to experiments may take place within the NFEM, this paper argues that, despite being a fully continuum model, the NFEM contains an intrinsic length scale—the Fermi wavelength  $\lambda_F$ —which, through electron-shell effects, provides some degree of “discreteness” for the ionic dynamics. The competition between surface and electron shell-effects favors the formation of kinks<sup>17</sup> in the wire radius, similar to the steps observed in experiments. The dynamics of these steps is shown to be in semi-quantitative agreement with experiments in many details. In particular, the model predicts an extremely fast nucleation and jump ahead of kinks at the wire end, followed by a regular, slower motion. Interactions between kinks, which can be either attractive or repulsive, profoundly affect their dynamics. For some wires, a kink is seen to be essentially stopped by its interaction with another one, until they combine and move as a single, larger kink, much like what is observed experimentally.<sup>5,6</sup>

The fast kink nucleation is found to be caused by the growth of an instability, and thus reminiscent of the dynamics of an unstable wire. The latter is thus discussed

and found to proceed through propagation of a pulled front into the unstable wire state.<sup>18</sup> A linear marginal stability analysis<sup>19</sup> of the front explains its dynamics in most cases. For some limited intervals of radius, a pushed front is found to result from the invasion of the linear front by a non-linear, marginally stable mode.<sup>20</sup>

The paper is organized as follows: In Sec. I, the NFEM is introduced and some of its main results directly relevant to the present article are summarized. The dynamics of an unstable cylinder, one with a non-magic radius, is discussed in Sec. II in terms of front propagation into an unstable state. This discussion, although not necessarily of direct experimental interest, provides useful insights into the formation of a kink, discussed in Sec. III, together with kink propagation and interactions between multiple kinks. Sec. IV discusses results and their relations to existing experiments.

## I. THE NANOSCALE FREE-ELECTRON MODEL

The NFEM is a continuum model of open metallic nanosystems with an emphasis on the electronic structure, which is treated exactly.<sup>13</sup> It is thus particularly suitable as a model of metal nanowires, and successfully describes many of their equilibrium<sup>11,13,15,21,22</sup> and dynamical<sup>10,14,16,17</sup> properties in simple physical terms.

The discrete atomic structure is replaced by a uniform, positively charged background (Jellium), which provides a confining potential for electrons. Electronic degrees of freedom are described using a free-electron model, thus neglecting interactions, except inasmuch as they rescale macroscopic quantities such as the bulk energy density  $\omega_B$ , and the surface tension  $\sigma_s$ .<sup>10,11,21</sup> This model is particularly suitable for simple metals, with good screening and a close-to-spherical Fermi surface, such as those with a single *s*-electron conduction band close to the Fermi surface. Such conditions are fulfilled for alkali metals like sodium, and to some extent for noble metals such as gold and silver.

While the NFEM has no such restriction, only axisymmetric wires are considered in this paper. This choice greatly simplifies the numerical treatment of the dynamics, as the wire shape can be described by a single radius function  $R(z, t)$ . It is justified by the facts that (i) the most stable wires are axisymmetric,<sup>23,24</sup> and (ii) the dynamics tends to decrease surface area, and thus further favors axisymmetric wires.

A nanowire being an open system, the electronic energy is given by the grand canonical potential  $\Omega_e$ . As any extensive thermodynamic quantity,  $\Omega_e$  can be written as a Weyl expansion<sup>25</sup>—a series in geometrical quantities such as system volume  $\mathcal{V}$  and surface area  $\mathcal{S}$ —complemented by a mesoscopic, fluctuating contribution  $\delta\Omega$ :

$$\Omega_e[R(z)] = \omega_B \mathcal{V} + \sigma_s \mathcal{S} + \delta\Omega, \quad (1)$$

where the values of  $\omega_B$  and  $\sigma_s$  may be chosen to match the bulk properties of the metal to be described. As results are independent on  $\omega_B$ , its free-electron value  $\omega_B = -2\epsilon_F k_F^3/15\pi^2$  is used, while the surface tension is set to  $\sigma_s = 1.256 \text{ N/m}$ , a value appropriate for the description of gold.<sup>26</sup>

Assuming the wire cross-section varies slowly along the wire (adiabatic approximation), the mesoscopic contribution may be written as

$$\delta\Omega[R(z)] = \int_0^L dz V_{shell}[R(z)], \quad (2)$$

where the electron-shell potential  $V_{shell}(R)$  can be computed using a semi-classical approximation.<sup>10</sup>  $V_{shell}(R)$ , depicted in Fig. 1 for a cylindrical wire as a function of its radius  $R$ , is responsible for stabilizing wires of magic radii, which correspond to its deep minima.

The ionic dynamics is classical and can be assumed to occur mainly through surface self-diffusion, as most atoms in thin metal wires are surface atoms.<sup>14,27</sup> The evolution equation for the radius function  $R(z, t)$  derives from ionic mass conservation

$$\frac{\pi}{\mathcal{V}_a} \frac{\partial R^2(z, t)}{\partial t} + \frac{\partial}{\partial z} J_z(z, t) = 0, \quad (3)$$

where  $\mathcal{V}_a = 3\pi^2/k_F^3$  is the volume of an atom, and the *z*-component  $J_z$  of the total surface current is given by

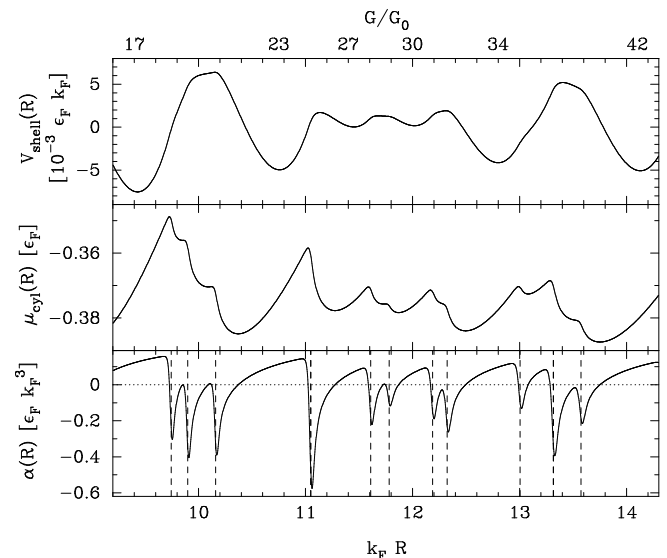


FIG. 1: Electron-shell potential  $V_{shell}(R)$  (top), chemical potential  $\mu_{cyl}(R)$  (middle), and stability coefficient  $\alpha(R)$  (bottom) for a cylindrical wire, as a function of its dimensionless radius  $k_F R$ , where  $k_F$  is the Fermi wavevector (The radius range is limited to that corresponding to simulation presented here. For a graph over a more extended range, see Ref. 14.) Vertical dashed lines in the bottom panel mark the positions of conductance channel openings, which drive the instability.<sup>13</sup> The top axis shows the conductance values of linearly stable cylinders in units of the conductance quantum,  $G_0 = 2e^2/h$ .

Fick's law:

$$J_z = -\frac{\rho_S D_S}{k_B T} \frac{2\pi R(z, t)}{\sqrt{1 + (\partial_z R)^2}} \frac{\partial \mu}{\partial z}. \quad (4)$$

Here  $\rho_S$  and  $D_S$  are, respectively, the surface density of ions and the surface self-diffusion coefficient,  $\partial_z R = \partial R / \partial z$ , and the ionic chemical potential  $\mu[R(z)]$  can be computed from the energy change due to the local addition of the volume  $\mathcal{V}_a$  of an atom to the system. It is found to be<sup>14</sup>

$$\mu[R(z)] = \mu_0 + \frac{\mathcal{V}_a}{2\pi R} \left( \frac{2\sigma_s \partial \mathcal{C}[R(z)]}{\sqrt{1 + (\partial_z R)^2}} + \frac{\partial V_{shell}}{\partial R} \right), \quad (5)$$

where  $\mu_0 = \omega_B \mathcal{V}_a$  is the bulk chemical potential. Here  $\partial \mathcal{C}[R(z)] = \pi \left( 1 - \frac{R \partial_z^2 R}{1 + (\partial_z R)^2} \right)$  is the local mean curvature of the wire. The chemical potential of a cylinder  $\mu_{cyl}(R) \equiv \mu[R(z) = R]$  is plotted as a function of the radius  $R$  in the middle panel of Fig. 1.

The precise value of  $D_S$  is not known for most metals, but it can be removed from the evolution equation by rescaling time to the dimensionless variable  $\tau = \omega_0 t$ , with the characteristic, temperature-dependent, frequency  $\omega_0 = \rho_S D_S T_F / T$ . For comparison to experimental time scales, one can estimate that for quasi-one-dimensional diffusion  $D_S \approx \nu_D a^2 \exp(-E_s / k_B T)$ , where  $\nu_D$  is the Debye frequency,  $a$  is the lattice spacing, and  $E_s$  is an activation energy comparable to the energy of a single bond in the solid.

Given the universality of a cylinder connected to leads as the equilibrium shape of a nanowire,<sup>14,16</sup> this paper focuses on the cylindrical part of the wire, of length  $L$ , leaving the connecting leads out of the system. In this case, Neumann boundary conditions,  $\partial_z R = 0$  at both ends of the wire,  $z = 0$  and  $z = L$ , are found to best describe the connection to the leads. The diffusive dynamics being volume conserving, a sink or source of atoms at one or both wire's end must be added to force the thinning or growth of the wire. This is done by adding a boundary current term to the r.h.s. of Eq. (3):

$$J_{bnd} = J_l \delta(z) - J_r \delta(z - L), \quad (6)$$

where a positive  $J_{l(r)}$  is a source of atoms at the left (right) wire end, while negative values correspond to sinks of atoms.

### Summary of previous results

A linear stability analysis of cylindrical wires has been performed within the NFEM.<sup>10,11,15,22</sup> The change in the energy (1) due to a radius perturbation  $\Delta R = \sum_q b_q \exp(iqz)$  was found to be,

$$\Delta \Omega_e = L \sum_q \alpha(R_0; q) |b_q|^2, \quad (7)$$

so that the sign of  $\alpha(R_0; q)$  determines the linear stability of a wire of radius  $R_0$  towards a perturbation of wavevector  $q$ . Hence  $\alpha(R_0; q)$  has been named the *stability coefficient*. It was further found that the global linear stability is essentially determined by the long wavelength limit<sup>11,15,22</sup>  $\alpha(R_0) \equiv \alpha(R_0; q = 0)$ , with

$$\alpha(R_0) = \left( -\frac{2\pi\sigma_S}{R} + \frac{d^2 V_{shell}}{dR^2} - \frac{1}{R} \frac{dV_{shell}}{dR} \right) \Big|_{R=R_0}. \quad (8)$$

Instabilities were found to result from a transverse eigenenergy of the wire crossing the Fermi energy  $\epsilon_F$ , thus closing or opening a conduction channel.<sup>13,15</sup> These thresholds are marked by vertical dashed lines in Fig. 1. Cylinders are linearly stable for intervals of *magic* radii, that roughly correspond to minima of the shell potential  $V_{shell}$ , while unstable wires correspond to maxima of  $V_{shell}$  (see Fig. 1). The stability coefficient  $\alpha(R)$  and chemical potential of a cylinder  $\mu_{cyl}(R)$  are related through<sup>10</sup>

$$\alpha(R) = \frac{2\pi R}{\mathcal{V}_a} \cdot \frac{d\mu_{cyl}(R)}{dR}. \quad (9)$$

A linearized dynamical theory<sup>11</sup> shows that unstable wires develop an exponentially growing instability with a well-defined wavelength  $\lambda = 2\pi/q_{max}$ , corresponding to the maximally unstable mode, such that  $\alpha(R_0; q_{max})$  is extremal. This instability was argued to saturate, and eventually lead to a phase separation of the wire into thick and thin segments of stable radii.<sup>11</sup> Simulations using the full dynamics (3) have confirmed this, and shown that the phase separation occurs via a complex dynamics involving kink interactions and annihilation.<sup>14</sup>

## II. INSTABILITY PROPAGATION

Results on the evolution of an unstable cylinder, including the growth of a single-wavelength perturbation followed by a phase separation, were briefly presented in a Letter.<sup>14</sup> In this section, I provide a more detailed analysis of the instability propagation, showing in particular that much of the dynamics derives from the linearized evolution equation, and is an example of front propagation into an unstable state.<sup>18,19</sup>

The initial condition for these simulations, where no boundary currents are used, is an unstable cylinder of radius  $R_0$ , i.e. a radius not in a magic interval, and length  $k_F L = 400$ . A Gaussian perturbation of amplitude  $k_F \delta R = 0.01$ , localized at the left boundary,  $z = 0$ , is added to trigger the instability. Results have been checked to be independent of the type, amplitude, and extension of the initial perturbation, as long as it is sufficiently localized.<sup>18</sup>

After a brief initial incubation period, during which the amplitude of the perturbation decreases, it increases exponentially and propagates along the wire. A well-defined front is formed and moves at a constant velocity

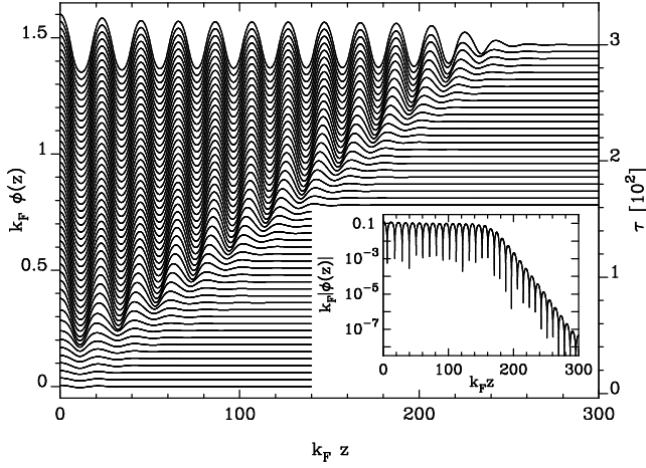


FIG. 2: Instability propagation for a wire of radius  $k_F R_0 = 11.65$ : The main panel shows  $\phi(z) = R(z) - R_0$  at equidistant times (shifted vertically upward for clarity), illustrating a typical time evolution of the stability propagation. In particular the coherent pattern left behind the front can be observed. The r.h.s. axis gives the dimensionless evolution time  $\tau$  for the corresponding curves. The inset shows  $|\phi(z)|$  at a given time,  $\tau \sim 180$ , on a logarithmic scale, illustrating its exponential decay ahead of the front.

(see Fig. 2). Behind the front, a coherent pattern consisting of a single-wavelength radius oscillation forms and saturates at an amplitude  $k_F \Delta\phi \sim 0.1-1$ , whose value depends on the details of the shell potential  $V_{shell}$  (cf Fig. 1) in the vicinity of the unstable radius  $R_0$  considered. Further evolution of the wire behind the front occurs on a timescale orders of magnitude longer than the front propagation. It involves annihilation of kink/antikink pairs—up- and down-ward steps in  $R(z)$ —and eventually leads to a phase separation in thick and thin segments of stable cylinders.<sup>11,14</sup> A similar, but simpler, kink dynamics is discussed in Sec. III.

A logarithmic plot of (the absolute value of) the wire perturbation  $\phi(z, t) = R(z, t) - R_0$  (see inset of Fig. 2, where  $k_F R_0 = 11.65$ ) clearly shows its exponential decay ahead of the front, whose position  $z_f$  is defined as the point where the perturbation amplitude reaches<sup>28</sup> a certain threshold value  $c$ . Tracking  $z_f$  as a function of time, the front velocity  $v$  can be extracted, and is found to be constant after an initial period when it is influenced by boundary and initial conditions. Similarly, the wavevector  $q$  and decay length  $\xi$  of the perturbation ahead of the front can be extracted. Both are found to be constant after an initial decrease during early evolution.

All three quantities, plotted as circles in Fig. 3, are found to depend non-trivially on the wire radius  $R_0$ . They reach local extrema simultaneously for values of  $R_0$  that correspond to minima of the stability coefficient  $\alpha$  (Fig. 1 and Eq. (8)), i.e. maximally unstable wires. The front velocity  $v$  and wavevector  $q$  vanish, while the decay length  $\xi$  diverges, at the stability boundary  $R_c$ , where  $\alpha(R_c) = 0$ .

Following ideas from linear marginal stability analysis of front propagation into unstable states,<sup>18,19</sup> much of the front dynamics can be understood from the linearized evolution equation for the perturbation  $\phi(z, t)$ ,

$$\frac{2\pi R_0}{\mathcal{V}_a} \frac{\partial \phi}{\partial t} = -\frac{\omega_0 \mathcal{V}_a}{\epsilon_F} \left[ 2\pi \sigma_s R_0 \frac{\partial^4 \phi}{\partial z^4} - \alpha(R_0) \frac{\partial^2 \phi}{\partial z^2} \right]. \quad (10)$$

Assuming a front of the form  $\phi(z, t) = \exp[i(\omega t - kz)]$ , with  $\omega$  and  $k$  complex quantities, its dispersion relation

$$\omega(k) = i \frac{\omega_0 \sigma_s \mathcal{V}_a^2}{\epsilon_F} k^2 \left( k^2 + \frac{\alpha(R_0)}{2\pi \sigma_s R_0} \right) \quad (11)$$

is derived. It has been argued<sup>19</sup> that the front wavevector  $k^*$  is such that the front is marginally stable, and thus satisfies the conditions<sup>18</sup>

$$\text{Im} \left. \frac{d\omega}{dk} \right|_{k^*} = 0, \quad \frac{\text{Im} \omega(k^*)}{\text{Im} k^*} = \left. \frac{d\omega}{dk} \right|_{k^*}. \quad (12)$$

This yields the front wavevector  $k^* \equiv q - i/\xi$ ,

$$k^* = \frac{1}{4} \sqrt{-\frac{\alpha(R_0)}{\pi \sigma_s R_0}} \left( \sqrt{3 + \sqrt{7}} - i \sqrt{\frac{\sqrt{7} - 1}{3}} \right), \quad (13)$$

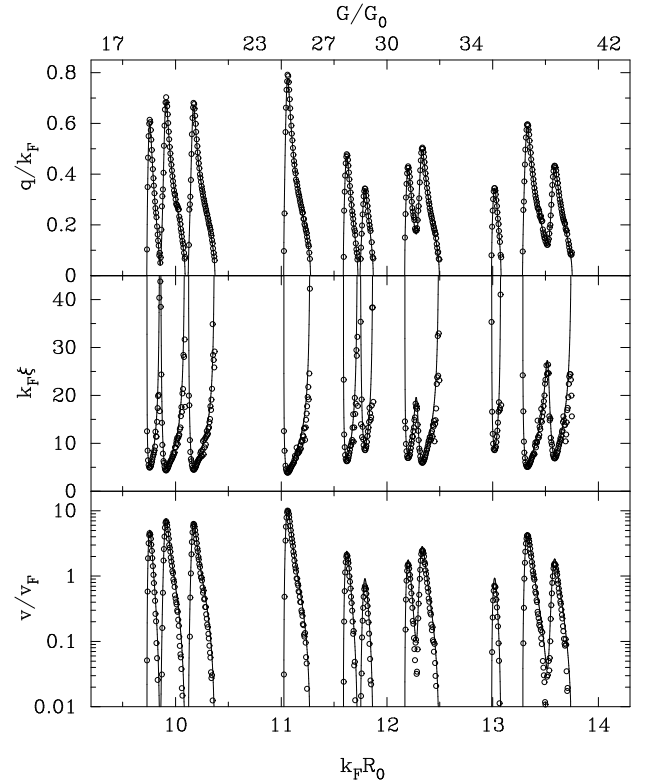


FIG. 3: Instability wavevector  $q$  (top), decay length  $\xi$  (middle), and front velocity  $v$  (bottom) as a function of unstable wire radius  $R_0$ . The solid lines give the results of the linear theory, Eqs. (13) and (15), and the circles are results extracted from the full dynamics simulations (Error bars are smaller than the symbols, and therefore not plotted.)

where the real part  $q$  determines the wavevector of the pattern left behind the front, and the inverse  $\xi$  of the imaginary part corresponds to the decay length ahead of the front. They are respectively plotted as solid lines in Fig. 3 (top two panels), and compare well with data extracted from the full non-linear dynamics (circles).

It is clear from Eq. (13) that the product

$$q\xi = \sqrt{\frac{3(3+\sqrt{7})}{\sqrt{7}-1}} \simeq 3.2, \quad (14)$$

is universal and does not depend on any wire parameters. This has been verified within numerical accuracy for all wire radii, as well as for two different values of  $\sigma_s$  (corresponding to Au and Na).

The front velocity  $v = \text{Im}[\omega(k^*)]/\text{Im} k^*$  is readily extracted from Eq. (13), and is found to be

$$v = \frac{\omega_0 \sigma_s \mathcal{V}_a^2}{6\epsilon_F} \sqrt{\frac{17+7\sqrt{7}}{3}} \left( -\frac{\alpha(R_0)}{\pi \sigma_s R_0} \right)^{3/2}. \quad (15)$$

This result is plotted in Fig. 3 (bottom panel) as a solid line, and compared with front velocities obtained from the dynamical simulations (circles). Agreement between the linear theory and full nonlinear dynamics is very good, showing that the front propagation is indeed governed by the linear dynamics.

Combining Eqs. (13) and (15), one gets

$$v \propto \sigma_s q^3, \quad (16)$$

so that the front velocity can be determined from the pattern wavelength. This relation also holds within numerical accuracy in simulations for Au and Na.

A closer look at the bottom panel of Fig. 3 shows some disagreement between the numerical and linear theory velocities  $v$  around  $k_F R_0 \simeq 12.3$  and  $k_F R_0 \simeq 13.5$ . This points to a breakdown of the linear marginal stability analysis<sup>19</sup> for these radii: A study of the shape evolution for these wires reveals that a front satisfying Eqs. (13–16) is formed and propagates for a while, but at some point a second, faster front emerges and takes over the first one, eventually dominating the dynamics. This “invading” front has a larger  $q$  and a smaller  $\xi$ , and satisfies neither Eq. (14), nor Eq. (16). This is consistent with the nonlinear marginal-stability mechanism discussed by van Saarloos,<sup>20</sup> where, for some range of parameters, the front becomes unstable to an “invasion mode”. In this case the evolution depends on the full nonlinear dynamics, and the front is “pushed” by the invading mode, rather than “pulled” by the exponentially growing instability.<sup>18</sup> The new front speed, wavevector and decay length seem consistent with the analysis of Ref. 20. Although the cause of the instability of the front to the invasive mode is not clear, it seems to be related to the existence of a “quasi-stable” wire, i.e. a wire for which  $\alpha(R)$ , though still negative, has a local maximum.

Finally, as  $\alpha(R) \propto \pm(R - R_c)$  at the stability boundaries, where  $\alpha(R_c) = 0$ , Eqs. (13) and (15) provide the

scaling of  $v$ ,  $q$ , and  $\xi$  with  $|R - R_c|$ . Their respective exponents are  $3/2$ ,  $1/2$  and  $-1/2$  as  $|R - R_c| \rightarrow 0$ .

As reported in Ref. 14, the evolution of the system after the instability propagation and saturation follows a complex dynamics that involves kink interactions and ‘fusion’, and leads to a phase separation of the wire into thin and thick stable wires.<sup>10,11</sup> This dynamics will be discussed in more details, starting with a simpler case, in the next section.

### III. KINK DYNAMICS

Once the instability has saturated in part of, or the whole wire, kinks, where the radius  $R(z)$  switches between two stable radii, interact with each other and annihilate in pairs of kink/antikink (one increasing the radius, while the other decreases it). This leaves longer and longer portions of the wire with a constant, stable radius. Eventually, this leads to a phase separation in thick and thin parts of the wire.<sup>11,14</sup> Many kink/antikink pairs being involved, the dynamics is rather complex. It is thus useful to consider a simpler setup, with a limited number of kinks, to study the kink dynamics and interactions. Such a setup, also motivated by the experimental observation of wire thinning by nucleation and motion of kinks,<sup>5</sup> consists of a cylindrical wire, initially of stable radius  $R_0$ , subjected to a boundary current that injects (source) or removes (sink) atoms into the system. As only wire thinning has been observed experimentally,<sup>5</sup> we will consider mainly the case of a sink of atom at the left end of the wire,  $J_l < 0$ .

Results of such a simulation are shown in Figs. 4, 6, and 7 for a wire of length  $k_F L = 150$ , with a boundary current  $J_l = -10^{-4} \pi \omega_0$ . Such a boundary current, following Eq. (4), creates a positive gradient of chemical potential  $\mu$  that progressively expands along the wire. This gradient corresponds roughly to a constant slope of  $R(z)$ , since a stable wire corresponds to a  $\mu_{cyl}(R)$  essentially linear in  $R$ . Once the global change in chemical potential is such that  $R$  crosses a minimum of  $\mu_{cyl}(R)$ , corresponding to a stability threshold (see Eq. (9) and Fig. 1), an instability sets in and forms a kink that will propagate along the wire. In most cases, like the transition from  $G/G_0 = 42 \rightarrow 34$  (Fig. 2), or  $G/G_0 = 23 \rightarrow 17$ , a single kink nucleates and propagates along the whole wire. Subsection III A discusses this case in details. Sometimes, however, a second kink nucleates before the first one has reached the end of the wire, as is the case in the transition  $G/G_0 = 34 \rightarrow 27 \rightarrow 23$ . If this happens, the two kinks interact attractively, and eventually combine and propagate as a single, larger kink (Figs. 6 and 7.) This is the simplest case of kink interaction, and is discussed in subsection III B.

The likelihood of a second kink being nucleated before the first reaches the wire end increases with the boundary current  $|J_l|$  and wire length  $L$ , but decreases with the wire stability. As mentioned previously, the chemical

potential profile on the left of the kink has a constant gradient, proportional to  $J_l$ , corresponding to a small gradient of  $R(z)$ . Inevitably, if the kink were propagating into an infinite wire, there would be a time  $\tau_n$  when the kink position  $z_k(\tau_n)$  is such that the potential difference due to this gradient is large enough for a new instability to set in, and thus a new kink to nucleate. If the wire length  $L$  is larger than  $L_c \equiv z_k(\tau_n)$ , this will happen even for a finite wire. The critical length  $L_c$  increases with the wire stability: A given drop  $\Delta\mu$  of the chemical potential may be enough to trigger nucleation of a new kink for a given wire, say one with  $G = 34 G_0$ , but not for a more stable wire, such as one with  $G = 27 G_0$  (see Fig. 1). As the gradient of chemical potential is proportional to the boundary current, Eq. (4), one clearly has  $L_c \propto |J_l|$ .

### A. Single kink evolution

The top panel of Fig. 4 displays the radius function  $R(z, \tau)$  at different evolution times (with alternately solid and dashed lines for clarity), with a dotted horizontal line showing the channel opening threshold, used to track the kink position  $z_k$ . The lower panel shows  $z_k$  as a function of time, both on linear (main plot) and log-log (inset) scales. One can clearly identify two phases with different time evolutions of the kink position: (i) the kink formation, during which  $z_k$  increases quickly, but the kink velocity decreases, and (ii) the kink propagation, when the kink moves without deformation at a constant velocity.

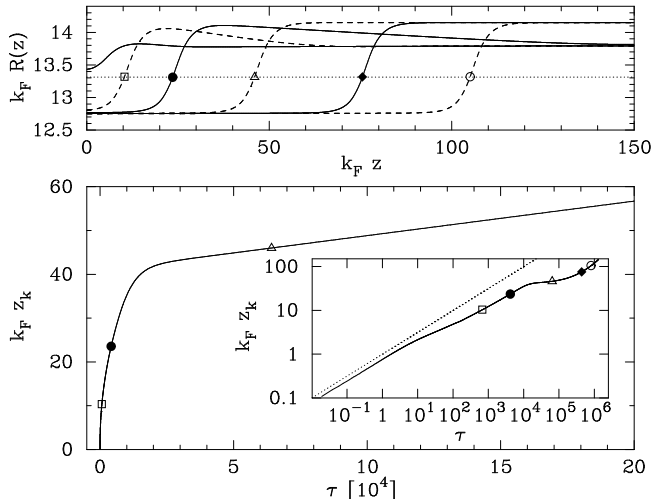


FIG. 4: (top) Radius function  $R(z)$  at various evolution times for a wire subject to a sink of atoms at  $z = 0$ . Solid and dashed lines are used on alternate curves for clarity, while the dotted line shows the threshold used to define the kink position. (bottom) Kink position  $z_k$  as a function of time on a linear and log-log (inset) scale. The kink position for the shapes plotted in the top panel are marked with corresponding symbols on each graph.

(i) *Kink formation:* As soon as a critical radius  $R_c$ , the limit between a stable and unstable zones where  $\alpha(R_c) = 0$ , is reached (first curve from the left in Fig. 4, top panel), an instability sets in and leads to the quick formation of a kink (2nd and 3rd curves from the left). During the kink formation, the radius “overshoots” ahead of the kink, and creates a “bump”, visible in the first dashed curve, which progressively extends over the whole wire (3rd and 4th curves from the left). The kink subsequently propagates without deformation (remaining curves) with a constant velocity, proportional to the boundary current  $|J_l|$ , provided the wire is stable enough, not too long, and the current small enough (see above).

The kink formation can be understood from the instability propagation described in Sec. II: Once the wire radius reaches an instability threshold  $R_c$ , an instability starts growing exponentially,  $\delta R \sim \exp[i(\omega t - kx)]$ , with  $\omega$  and  $k$  given by Eqs. (11) and (13) respectively. Since the (unstable) radius at the wire’s left end changes with time, the dynamics of the instability propagation is more involved than in Sec. II, and it is not clear which wavevector, if any, dominates. Let us assume that it is the case anyway. Although there is no well-defined kink at this point, its position can be defined as the point where  $\delta R$  reaches a fixed value  $\delta$ . Results depend weakly on that value,<sup>18</sup> which is chosen to be the threshold for conduction band closing.

Solving  $\delta R(z_k, \tau) \equiv \delta$  for small  $qz_k(\tau)$ , the kink position during its formation is found to be

$$k_F z_k(\tau) \propto \sqrt{\tau - \tau_0}, \quad (17)$$

where  $\tau_0$  is the kink formation (dimensionless) time. This result is independent of the boundary current, as long as the later is sufficiently small compared to the growth rate of the instability. This behavior of the kink position is observed only in the early stages of the kink formation,  $\Delta\tau = \omega_0(t - t_0) \lesssim 2$ , as can be seen in the inset of Fig. 4, where  $\sqrt{\tau}$  has been plotted as a dotted line for comparison.

As happens for the instability of an unstable cylinder, the growth saturates once it reaches the next minimum of  $V_{shell}$ , leaving a well-formed kink. As shown by the linear theory of Sec. II, the product of the decay length and wavevector, Eq. (14), is a constant  $q\xi \simeq 3.2$ , so that the instability is only visible over essentially one wavelength  $\lambda$ . Its first half wavelength becomes the kink, while the second half-wavelength, much reduced in amplitude, is responsible for the observed overshoot. This “bump” is found to spread in time over the whole wire, meanwhile speeding up the kink propagation, as will be discussed in the next paragraph.

(ii) *Kink propagation:* The kink propagation can be fully understood from the fact that the evolution Eq. (3) is volume conserving, once it is realized that the kink propagates without deformation. The chemical potential along the wire during bump propagation is depicted schematically in Fig. 5(a). It is constant, or has a constant slope proportional to the boundary current,

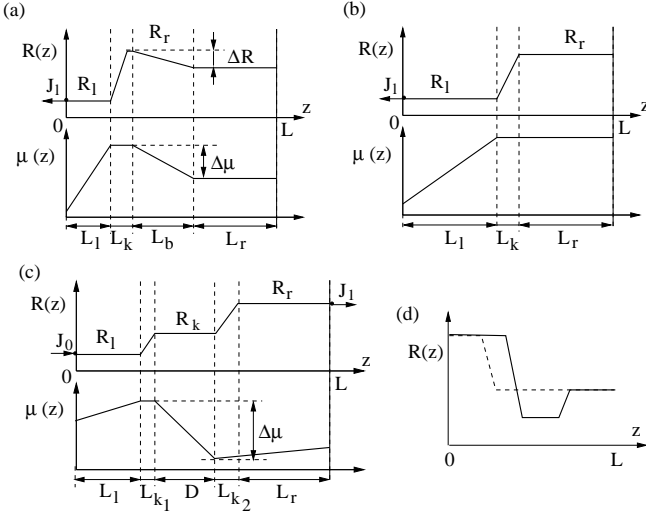


FIG. 5: Schematic diagram of the radius function  $R(z)$ , and corresponding chemical potential  $\mu(z)$ , during (a) the bump propagation ahead of a kink, (b) a kink propagation, (c) interaction of two kinks, and (d) interaction of a kink and antikink. The diagrams define the radii and lengths used in the text, as well as the chemical potential drop  $\Delta\mu$ . The arrows labeled  $J_\kappa$  mark the position of the sinks or sources of atoms. In panel (d), only the radius function is shown, and the dashed line represents  $R(z)$  before nucleation of the second kink.

in cylindrical parts of the wire, i.e. to the left of the kink and to the right of the bump. It is essentially constant over the kink, and drops by an amount  $\Delta\mu < 0$ , constant during evolution, over the extent of the bump. Consequently, the gradient of potential  $\Delta\mu/L_b$  over the bump, where  $L_b$  is the length of the bump, decreases (in absolute value) with time.

Let us consider a portion of the wire of length  $L_0 > L_b$  starting at the maximum of the bump, of radius  $R_r$ . Its volume is  $V_0 = \pi[(R_r - \Delta R/2)^2 L_b + (R_r - \Delta R)^2 (L_0 - L_b)]$ , where  $\Delta R > 0$  is the radius drop over the extent of the bump.  $V_0$  increases over time due to a positive current  $J = -2\pi\omega_0 R_r \Delta\mu/L_b$  on its left side, while there is no current on its r.h.s. Volume conservation for that portion of the wire provides a differential equation for  $L_b(\tau)$ , which yields  $L_b(\Delta\tau) = l_b \sqrt{\Delta\tau}$ , where  $\Delta\tau$  is the time measured from the bump formation, and

$$l_b^2 = -\frac{4V_a R_r \Delta\mu}{\epsilon_F \Delta R (R_r - 3\Delta R/4)}. \quad (18)$$

Eq. (18) depends only on a small number of geometrical parameters that can be read off  $R(z, \tau)$  at any given time during bump propagation. Even  $\Delta\mu = \mu_{cyl}(R_l) - \mu_{cyl}(R_r - \Delta R)$  can be read from Fig. 1.

The time evolution of the kink displacement  $\Delta z_k(\Delta\tau = \tau - \tau_1) \equiv z_k(\tau) - z_k(\tau_1)$ ,  $z_k$  being the kink position, during the bump propagation, derives from volume conservation for the whole wire, and is

$$\Delta z_k(\Delta\tau) = \frac{\Delta R (R_r - \frac{3\Delta R}{4}) l_b \Delta\tau^{1/2} - \frac{V_a J_l}{\pi\omega_0} \Delta\tau}{(R_r - \Delta R)^2 - R_l^2}. \quad (19)$$

In the present simulation,  $J_l/\omega_0 \ll 1$ , so that the corresponding term in Eq. (19) may be neglected, and only the  $\sqrt{\Delta\tau}$  behavior is observable, as can be seen in the inset of Fig. 4 for  $10^2 \lesssim \tau \lesssim 10^4$ .

How far the kink moves during the bump propagation, as well as how long it takes for the bump to reach the wire end, can be estimated from  $\Delta z_k(\Delta\tau_{bump}) + L_b(\Delta\tau_{bump}) \sim L$ . It is found that  $\Delta z_k(\Delta\tau_{bump}) \simeq \eta L$ , with a proportionality constant  $\eta$  depending on the coefficients of  $\Delta\tau$  and  $\sqrt{\Delta\tau}$  in Eq. (19). For most kinks,  $\eta \sim 0.1 - 0.3$ . The propagation time  $\Delta\tau_{bump}$  is also proportional to  $L$ , and is found to be of order  $10^3 - 10^4$ . For the kink of Fig. 4, the constant is  $\eta \simeq 0.14$ , so that the kink jumps ahead by about  $k_F \Delta L \simeq 20$  during this phase, that lasts a time  $\Delta\tau_{bump} \simeq 4 \cdot 10^3$ , in agreement with the simulation.

Once the bump has reached the end of the wire, the chemical potential profile becomes simpler, and is then constant for  $z > z_k(\tau)$ , as depicted schematically in Fig. 5(b). The same volume conservation argument shows that the kink moves with a constant speed determined by the radii on both end of the wire, and proportional to the boundary current:

$$z_k(\tau) = z_k(\tau_1) - \frac{V_a}{\pi(R_r^2 - R_l^2)} \frac{J_l}{\omega_0} (\tau - \tau_1), \quad (20)$$

where  $\tau_1$  is the time at which the bump has been fully absorbed at the wire end. The kink velocity obtained from Eq. (20) is in good agreement with the slope of Fig. 2.

## B. Multiple kinks: Interactions

Figure 6 traces the positions of two interacting kinks during the transition from  $G/G_0 = 34$  to 23, via 27 that occurs later in the simulation discussed above. The newly nucleated kink, appearing around  $\tau = 10^6$  (dashed line), slows down and even reverses (see inset) the motion of the existing kink (solid line). After they interact, both kinks appear to move in parallel at a constant speed. In fact, following the radius function  $R(z, \tau)$  during evolution, plotted vertically with a rightward shift proportional to  $\tau$  in Fig. 7, reveals that the two kinks combine to form a larger one. The relative speed of both kinks increases as they get closer, as revealed by a plot of the evolution of the interkink distance  $D$  (dotted line in inset of Fig. 6).

The interaction between any two kinks can be understood in simple terms when both kinks are well formed and separated enough, i.e. each of them propagates without deformation and all bump propagation is over. In that case, the kinks connect approximately cylindrical segments of wire with respective radii  $R_l$ ,  $R_k$ , and  $R_r$ , as depicted schematically in Fig. 5(c). According to Eq. (4), the chemical potential profile on either side of the pair of kinks has slopes proportional to the currents  $J_0$  and  $J_1$  on the left and right hand sides of the kinks respectively, which are assumed to be known. There is in general a linear change of the potential  $\Delta\mu = \mu_{cyl}(R_l) - \mu_{cyl}(R_r)$

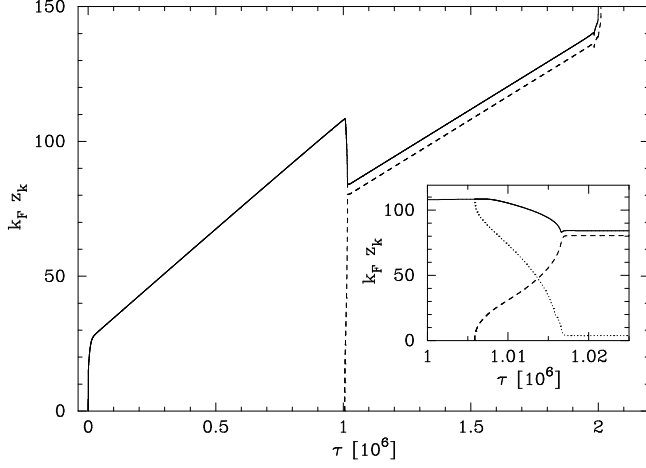


FIG. 6: Evolution of the kink positions for two interacting kinks in a wire subjected to a sink of atoms at its left boundary. The wire radius before nucleation of the first kink ( $\tau < 0$ ) is  $k_F R = 12.75$ , corresponding to a conductance  $G = 34G_0$ , and the wire thins down to  $k_F R = 10.7$ , and  $G = 23G_0$ , by the time the ‘combined’ has reached the wire’s end. The inset zooms in on the time region where two kinks interact ( $\tau \simeq 10^6$ ), with the dotted line showing the distance  $\Delta z$  between the two kinks.

over the segment of the wire, of length  $D$ , joining the two kinks. Considering mass conservation separately for two portions of wire containing respectively only the first and second kink, and combining the two equations thus obtained, the following differential equation for the distance  $D$  between the kinks is obtained:

$$\frac{\pi}{\mathcal{V}_a} \frac{dD}{dt}(t) = \frac{J_0}{R_k^2 - R_l^2} + \frac{J_1}{R_r^2 - R_k^2} + \frac{2\pi\omega_0}{\epsilon_F} \frac{R_k(R_r^2 - R_l^2)}{(R_r^2 - R_k^2)(R_k^2 - R_l^2)} \frac{\Delta\mu}{D(t)}. \quad (21)$$

As long as the outside currents  $J_0$  and  $J_1$  are small enough, the last term in Eq. (21) dominates, so that  $D^2(t) \propto (t - t_0)$ . The proportionality constant can have either sign depending on the balance of chemical potentials of the outside cylinders, as well as the type of both kinks (upward or downward steps). The interaction force between kinks can thus be attractive or repulsive. It can be calculated as  $F = -\frac{\partial\Omega_e}{\partial D}|_V$ , where  $\Omega_e$ , given by Eq. (1), is the energy of a portion of the wire containing both kinks. The result is

$$F = \varepsilon(R_k) - \frac{R_r^2 - R_k^2}{R_r^2 - R_l^2} \varepsilon(R_l) - \frac{R_k^2 - R_l^2}{R_r^2 - R_l^2} \varepsilon(R_r), \quad (22)$$

where  $\varepsilon(R) = 2\pi\sigma_s R + V_{shell}(R)$ . The interaction force between two kinks is thus *constant*, independent of their separation!

Coming back to the kinks of Fig. 6, their interaction is found to be attractive, as expected from their observed behavior. Even for the largest kink separation, of order

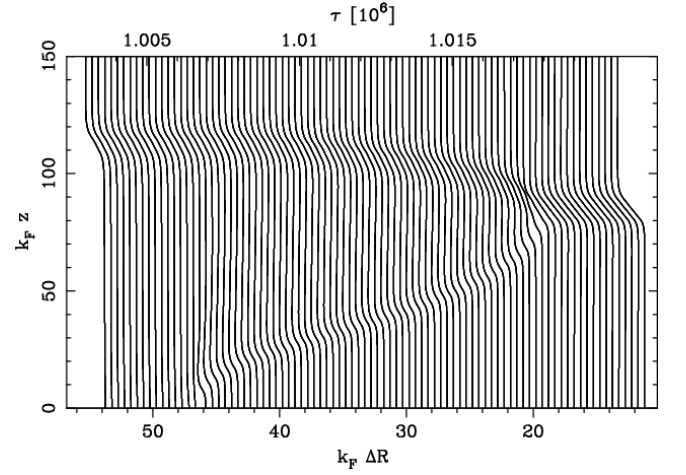


FIG. 7: Radius function  $R(z)$  at equidistant times  $\tau$ , showing the nucleation of a second kink (dashed line in Fig. 6) that interacts and fuses with the preexisting kink around  $\tau \simeq 1.016 \cdot 10^6$ .  $R(z)$  is plotted vertically, with a rightward shift proportional to the evolution time, for better comparison with the inset of Fig. 6.

$k_F D \sim 100$ , the last term of Eq. (21) is still one order of magnitude larger than the other terms, which may thus be neglected. Solving for  $D(t)$ , one gets an evolution in agreement with the dotted line in Fig. 6. The time evolution for the kink positions  $z_{k_1}(\tau)$  and  $z_{k_2}(\tau)$  can be extracted by considering volume conservation for the whole wire. Results are found to be in agreement with the simulation.

A simple case of repulsive interaction between two kinks is obtained by replacing the sink of atoms by a source,  $J_l > 0$ . While during wire thinning, the slightly stable wire at  $G = 30G_0$  was skipped, or more exactly a new kink was nucleated so quickly that that radius was only observable for a very short time, it is observed during wire growth. When the kink to  $G = 34G_0$  is nucleated, its amplitude is large enough that the bump ahead of the kink—which is now towards lower radii, and thus more of a hole—is large enough to trigger an instability towards lower radii. This forms an additional kink ahead of the existing one, as schematically shown in Fig. 5(d). In that particular case, the dynamics is found to be dominated by the interkink force (22) only in the very early stages of evolution, while the external current quickly provides deviations from the  $t^{1/2}$  behavior of the interkink distance. Interestingly, the contribution of the outside current  $J_0 = J_l$  is attractive, so that the sign of the global force changes sign when the kinks are far apart, and the interkink distance oscillates with time (as long as no other kink is nucleated.)

Finally, Eq. (22) allows a simple prediction about the long-time dynamics of unstable wires—after the instability has propagated throughout the wire. In that case, the kinks switch back and forth between two neighboring stable radii, so that Eq. (22) simplifies to  $F = \varepsilon(R_k) - \varepsilon(R_o)$ ,



where  $R_k$  and  $R_o$  are respectively the radii between and outside the two kinks considered. When  $F > 0$ , the cylinder between the two kinks behaves exactly as a *false vacuum*. As a result, if one considers kinks switching between radii corresponding to conductances  $G/G_0 = 23$  and 27, the kink interaction will tend to decrease the interkink distance for segments of the larger radius, while the opposite is true for oscillations between  $G/G_0 = 30$  and 34. This is confirmed by long-time simulations.

The general evolution of a system with multiple kinks/antikinks can be predicted by considering each pair of neighboring kinks separately. A set of differential equations similar to Eq. (21) is thus obtained for each interkink distance, and may be solved, together with an additional equation from global volume conservation, for each kink position. A general trend of the kink dynamics is to decrease the number of kinks, and increase the length of cylindrical segments.

#### IV. DISCUSSION AND CONCLUSIONS

The previous sections have presented detailed results on the dynamics of a metal nanowire within the NFEM under various conditions, all of which exhibit a rich kink dynamics. The evolution of unstable wires, discussed in Sec. II, provides an interesting system where ideas developed in the context of front propagation into an unstable state<sup>18,19,20</sup> can be successfully tested. The instability is found to grow exponentially ahead of a well-defined front, leaving a coherent pattern behind it. In most cases, the front is found to be pulled by the instability growth ahead of it. Its propagation is thus governed by the linearized evolution equation (10). Simple expressions for the front velocity  $v$  and decay length  $\xi$ , as well as the pattern wavevector  $q$  have been derived, and found to be in good agreement with numerical simulations using the full non-linear dynamics.

In other rare cases, the linear evolution equation (10) fails to explain the front dynamics. The pulled front is found to be invaded by a faster instability that pushes the front at its higher velocity. In this case, the front parameters depend on the full non-linear dynamics. The presence of an invading mode seems to correspond to quasi-stable wires, for which  $\alpha(R_0)$  is still negative, but has a local maximum close to 0.

Experimental verification of the dynamics of an unstable wire would be difficult, but may be, at least in part, possible. An unstable cylinder can be prepared using a potential bias: As the magic radius intervals vary with a bias applied along the wire,<sup>29</sup> a stable cylindrical wire can be prepared at a finite bias  $V$ , and its stability modified by suddenly switching the bias off. If the bias and wire radius are chosen appropriately, the wire becomes unstable, and its dynamics can be observed using, for example, transmission electron microscopy.<sup>1</sup> The connection of the wire to macroscopic leads acts as a localized perturbation at the end of the wire triggering the instability propaga-

tion. Actual observation of the front propagation would however be difficult as wire imperfections are likely to trigger the instability at several places along the wire simultaneously. In addition, the experiment needs to be conducted at room temperature for the metal to be soft enough to allow surface diffusion, so that thermal fluctuations are likely to have the same effect. Furthermore, the predicted radius oscillations are of the same size as the atomic granularity, and the two may thus be difficult to distinguish.

On the other hand, the kink dynamics described in Sec. III is much more accessible to experiments, and has in fact already been observed for gold<sup>5</sup> and silver<sup>4</sup> wires in TEM experiments: Movies of the real-time dynamics of gold wires<sup>6</sup> show a step-wise thinning of a cylindrical wire from 7 down to 4 atomic diameters, through motion of steps along the wire. Steps are seen to nucleate and move very rapidly—faster than the time resolution of the experiment—across a significant portion of the wire, much in agreement with the fast initial propagation predicted during kink formation and bump propagation in the NFEM. Some steps are seen to stop along the way, as during the transition from 6 to 4 atomic diameters. A second step appears to join the first one, before they move along. All this is in semi-quantitative agreement with simulations presented in Sec. III as the starting wire with a conductance  $G = 42 G_0$  (Fig. 4) has a diameter close to 7 atomic diameters, while a wire with a conductance of  $17 G_0$  corresponds to 5 atomic diameters. Note that conductance values quoted here are quantized values corresponding to ideal, ballistic transport. Measured conductances<sup>30</sup> are likely to be lower due to backscattering of electrons<sup>31</sup> from wire imperfections and disorder in the leads.

The simulation includes a sink of atoms, modeled as a constant boundary current. This is meant to mimic the experimental observation that wires thin down, presumably due to thermal fluctuations, electron irradiation from the electron microscope, and/or tensions on the wire. Thermal fluctuations of the boundary current would provide fluctuations around the ideal dynamics discussed here, but are not expected to alter it significantly. The effect of thermal fluctuations of the whole wire structure have been studied using a stochastic dynamical model.<sup>17</sup> The escape mechanism from long, metastable cylinders is found to be the nucleation of a kink at the wire end, that propagates along the cylinder. Thermal fluctuations may thus be included as a random fluctuation of the boundary current. Finally, a single sink of atoms is used in order to simplify the dynamics. When two sinks of atoms are included, the dynamics is found to be dominated by the larger one: Kinks nucleate at the position of the larger boundary current, and propagate through most of the wire before the other sink nucleates the corresponding antikink. The thinning dynamics with two, unequal sinks of atoms is thus essentially equivalent to that of a single kink, except for the absorption at the wire end.

The NFEM is a fully continuous model that exhibits some degree of “discreteness”, apparent through the formation of kinks connecting cylindrical parts of the wire. Although the dynamics of the ionic background is fully classical in the NFEM, it is strongly influenced by the electron-shell potential, which is a result of the quantum confinement of the transverse motion of the electrons within the wire. The latter provides a “quantization” of the continuous ionic structure on a scale given by the Fermi wavelength  $\lambda_F$ , and is responsible for the rich kink dynamics.

The NFEM assumes that the atomic structure of the wire adapts itself to the shape dictated by the electronic structure. One of the main drawback of this assumption is that it neglects any possible back-action of the atomic structure on the electronic motion. However these effects, though hard to evaluate, are expected to be minimal for the wires considered in this paper, which are thin enough that crystalline structure is not expected—and is indeed not observed<sup>1,2</sup>—but thick enough for a continuous approximation to be reasonable.

The very simplicity of the model makes simulations of large systems over long times tractable. The initial wire for the simulation of Sec. III corresponds to  $4 \cdot 10^4$  atoms, over an evolution time of seconds. This is far beyond what any simulation based on more “realistic” models, such as *ab initio*<sup>7</sup> or classical molecular dynamics<sup>8</sup> simulations, can hope to achieve in the foreseeable future,

as they are currently limited to at most a few nanoseconds. Furthermore, classical molecular dynamics simulations, which can treat relatively large systems, do not include electron-shell effects, and are therefore unable to even stabilize a long nanocylinder. The NFEM—with all its simplifying assumptions, and thanks to them—is to date the only model allowing realistic predictions of the long-time dynamics of metal nanowires. As the latter is now accessible experimentally with an atomic resolution, these predictions can be tested and falsified.

Finally, although the NFEM is in principle limited to simple free-electron-like metals, such as the alkali, and to some extent noble metals, confinement of the electronic transverse motion is a very general feature of metals as soon as the transverse linear dimension of the system is of the order of the Fermi wavelength. As such, its consequences, from the magic radii for the stability to the “discreteness” of the ionic dynamics, are expected to be quite general.

### Acknowledgments

I am grateful to Profs. Charles Stafford and Ray Goldstein for enlightening discussions on various aspects of this research. This work is supported by NSF grants 0312028 and 0351964.

---

\* Electronic address: buerki@physics.arizona.edu

<sup>1</sup> Y. Kondo and K. Takayanagi, Phys. Rev. Lett. **79**, 3455 (1997).

<sup>2</sup> Y. Kondo and K. Takayanagi, Science **289**, 606 (2000).

<sup>3</sup> V. Rodrigues, T. Fuhrer, and D. Ugarte, Phys. Rev. Lett. **85**, 4124 (2000).

<sup>4</sup> V. Rodrigues, J. Bettini, A. R. Rocha, L. G. C. Rega, and D. Ugarte, Phys. Rev. B **65**, 153402 (2002).

<sup>5</sup> Y. Oshima, Y. Kondo, and K. Takayanagi, J. Electron Microsc. **52**, 49 (2003).

<sup>6</sup> Real-time movies of nanowire dynamics are available online at K. Takayanagi’s group web page, [http://wwwsurf.phys.titech.ac.jp/tylab/index\\_e.html](http://wwwsurf.phys.titech.ac.jp/tylab/index_e.html).

<sup>7</sup> E. Z. da Silva, F. D. Novaes, A. J. R. da Silva, and A. Fazzio, Phys. Rev. B **69**, 115411 (2004).

<sup>8</sup> S. J. A. Koh and H. P. Lee, Nanotech. **17**, 3451 (2006).

<sup>9</sup> S. Chandrasekhar, *Hydrodynamic and hydromagnetic stability* (Dover, New York, 1981).

<sup>10</sup> J. Bürki and C. A. Stafford, Appl. Phys. A **81**, 1519 (2005).

<sup>11</sup> C.-H. Zhang, F. Kassubek, and C. A. Stafford, Phys. Rev. B **68**, 165414 (2003).

<sup>12</sup> M. Brack, Rev. Mod. Phys. **65**, 677 (1993).

<sup>13</sup> C. A. Stafford, D. Baeriswyl, and J. Bürki, Phys. Rev. Lett. **79**, 2863 (1997).

<sup>14</sup> J. Bürki, R. E. Goldstein, and C. A. Stafford, Phys. Rev. Lett. **91**, 254501 (2003).

<sup>15</sup> F. Kassubek, C. A. Stafford, H. Grabert, and R. E. Goldstein, Nonlinearity **14**, 167 (2001).

<sup>16</sup> J. Bürki, *Nonlinear Dynamics of Metallic Nanofabrication*

(Techna Group Srl, Faenza, Italy, 2004), vol. 44 of *Advances in Science and Technology*, pp. 185–192.

<sup>17</sup> J. Bürki, C. A. Stafford, and D. L. Stein, Phys. Rev. Lett. **95**, 090601 (2005).

<sup>18</sup> W. van Saarloos, Phys. Rep. **386**, 29 (2003).

<sup>19</sup> W. van Saarloos, Phys. Rev. A **37**, 211 (1988).

<sup>20</sup> W. van Saarloos, Phys. Rev. A **39**, 6367 (1989).

<sup>21</sup> F. Kassubek, C. A. Stafford, and H. Grabert, Phys. Rev. B **59**, 7560 (1999).

<sup>22</sup> D. F. Urban and H. Grabert, Phys. Rev. Lett. **91**, 256803 (2003).

<sup>23</sup> D. F. Urban, J. Bürki, C.-H. Zhang, C. A. Stafford, and H. Grabert, Phys. Rev. Lett. **93**, 186403 (2004).

<sup>24</sup> D. F. Urban, J. Bürki, A. I. Yanson, I. K. Yanson, C. A. Stafford, J. M. van Ruitenbeek, and H. Grabert, Solid St. Comm. **131**, 609 (2004).

<sup>25</sup> M. Brack and R. K. Bhaduri, *Semiclassical physics*, vol. 96 of *Frontiers in physics*, Ed. by D. Pines (Addison-Wesley, 1997).

<sup>26</sup> W. R. Tyson and W. A. Miller, Surf. Sci. **62**, 267 (1977).

<sup>27</sup> For example, more than 60% of the atoms of a wire with a diameter of 6 atomic layers, corresponding to a conductance around  $30 G_0$ , are at the wire’s surface.

<sup>28</sup> The front position thus defined is somewhat arbitrary, but results for the front velocity are independent of the choice of  $c$ <sup>18</sup>.

<sup>29</sup> C.-H. Zhang, J. Bürki, and C. A. Stafford, Phys. Rev. B **71**, 235404 (2005).

<sup>30</sup> Y. Oshima, K. Mouri, H. Hirayama, and K. Takayanagi,

- J. Phys. Soc. Japan **75**, 053705 (2006).  
<sup>31</sup> J. Bürki, C. A. Stafford, X. Zotos, and D. Baeriswyl, Phys. Rev. B **60**, 5000 (1999).